The spatial-temporal total friction coefficient of the fault viewed from the seismo-electromagnetic theory.

Patricio Venegas-Aravena (1, 2), Enrique G. Cordaro (2, 3), David Laroze (4).

(1) Department of Structural and Geotechnical Engineering, School of Engineering, Pontificia Universidad Católica de Chile, Vicuña Mackenna 4860, Macul, Santiago, Chile.
(2) Cosmic Radiation Observatories, University of Chile, Casilla 487-3, Santiago, Chile
(3) Facultad de Ingeniería, Universidad Autónoma de Chile, Pedro de Valdivia 425, Santiago, Chile.
(4) Instituto de Alta Investigación, CEDENNA, Universidad de Tarapacá, Casilla 7D, Arica, Chile.

Author: P. Venegas-Aravena: plvenegas@uc.cl
Co-author: E. G. Cordaro: ecordaro@dfi.uchile.cl
Co-author: D. Laroze: dlarozen@uta.cl

Abstract

Recently, it has been shown theoretically how the lithospheric stress changes could be linked with magnetic anomalies, frequencies, spatial distribution and the magnetic-moment magnitude relation using the electrification of microfractures in the semi brittle-plastic rock regime [Venegas-Aravena *et al*. Nat. Hazards Earth Syst. Sci. **19**, 1639 – 1651 (2019)]. However, this Seismo-electromagnetic Theory has not been connected with the fault's properties in order to be linked with the onset of the seismic rupture process itself. In this work we provide a simple theoretical approach to one of the key parameters for seismic ruptures as the friction coefficient and the stress drop. We use sigmoidal functions to model the stress changes in the non-elastic regime within lithosphere. We determine the temporal changes in frictional properties of faults. We also use a long-term friction coefficient approximation that depends on the fault dip angle, and four additional parameters that weigh the first and second stress derivative, the spatial distribution of the non-constant stress changes and the stress drop. We found that the friction coefficient is not constant in time and evolves prior and after the earthquake occurrence regardless of the (non-zero) weight used. When we use a dip angle close to 30 degrees and the contribution of the second derivative is more significant than the first derivative, the friction coefficient increases prior to the earthquake. During the earthquake event the friction drops. Finally, the friction coefficient increases and decreases again after the earthquake occurrence. Important to mention that when there is no contribution of stress changes in the semi brittle-plastic regime, no changes are expected in the friction coefficient.

Keywords: Seismo-electromagnetic Theory, Friction coefficient, Magnetism, Earthquakes, LAIC effect.

1.- Introduction

The electromagnetic phenomena that could be linked with earthquake occurrences are usually considered within the lithosphere-atmosphere-ionosphere-coupling effect (or LAIC effect) (e.g. De Santis et al., 2019a). Some of these electromagnetic phenomena have been recorded both prior and after the earthquakes using different methodologies, data, earthquakes and instrumentation. For example, some researchers have shown co-seismic magnetic variations during some earthquakes (e.g. Utada et al. (2011) during Tohoku 2011 earthquake). While others researches have been focusing on the oscillation frequency ($\mu Hz - kHz$ range) of magnetic field prior to the occurrence of some earthquakes (Schekotov and Hayakawa, 2015; Cordaro et al., 2018; Potirakis et al., 2018a, b, among other). One of the most recent methodology corresponds to the measurement of magnetic anomalies, which detects the number of

magnetic peaks (or events) that exceed a given threshold that represents the normal conditions of the magnetic field during long periods of time (De Santis et al., 2017). There is some research that shows that the increases in the number of anomalies could be linked with the impending earthquakes. For instance, De Santis et al. (2019b) have recently found an increase in the amount of daily magnetic anomalies prior to 12 major earthquakes between 2014 and 2016. These magnetic anomalies were confirmed by other researchers (e.g. Marchetti and Akhoondzadeh (2018)).

It is well known from laboratory experiments that rock samples undergoing fast changes in the semi brittle-plastic rock regime generate microfractures, displacement of dislocations and electrification (e.g. Anastasiadis et al., 2004). This physical mechanism of rock electrification is described mathematically by The Motion of Charged Edge Dislocations (MCD) model (e.g. see Vallianatos and Tzanis (1998) or Vallianatos and Tzanis (2003) for a comprehensive derivation of the MCD model). This model is a plausible electromechanical mechanism that could explain the magnetic measurements. Starting from the experimental evidences Venegas-Aravena et al. (2019) developed a Seismo-electromagnetic Theory based on microcracks and stress changes. This theory showed how the fractal nature of the cracks explains the observed magnetic frequency range, the co-seismic magnetic field and the conditions for generating magnetic anomalies. However, this theory (neither the others, e.g. Freund, 2003, De Santis et al., 2019a) does not explain any change on the parameters that control the generation of seismic ruptures using magnetic measurements. This prevents to link the seismo-electromagnetism and the classical seismology. In this work, we address this link using one of the key points that control seismic rupture and slip on the fault: friction force and stress drop. Our model uses the tectonic geometry and stress drop of Maule 2010 Mw8.8 earthquake in order to provide real data and validate our analysis. The paper is divided as follows, in section 2 we consider the friction coefficient adding the brittle-plastic stress changes contribution to the usual elastic stress. In section 3 we discuss the temporal variations of the brittle-plastic friction and their connections with the spatial distribution on the fault and the lithosphere. In section 4 we provide the relation between the stress drop and the co-seismic magnetic field. The spatial-temporal friction coefficient along the fault is calculated by adding the elastic stress drop. In section 5, the Gutenberg-Richter's law is written in terms of the semi brittle-plastic shear stress. The rupture time is discussed in section 6. Finally, the discussion and conclusions are drawn in section 7.

2. - Friction coefficient in the brittle-plastic regime

The standard friction force can be understood as the complex dissipation of mechanical energy in the form of plastic or elastic deformation of asperities (mechanical interaction), thermal dissipation (heat) and the adhesion (interatomic interaction) of two sliding surfaces (e.g. Sun and Mosleh, 1994). When we consider a particular contact area between two dry surfaces, the static friction coefficient μ that describes this interaction can be written approximately as the ratio of the shear τ and the normal N stress (load) as shown by Equation (1) (e.g. Byerlee, 1978, Chen, 2014, and references therein).

$$\mu = \frac{\tau}{N}. \qquad (1)$$

The static friction coefficient μ gives some information about the contact behavior. For instance, μ tends to be large when the contact area is increased due to the surface's plastic deformation (e.g. Chen, 2014). If we also consider the pure plastic regime, we can add a small plastic shear stress ($\delta\tau_{plastic}$) and a small plastic normal stress ($\delta N_{plastic}$) contribution in Equation (1) leading to the following expressions:

$$\tau = \tau_{elastic} + \delta\tau_{plastic}. \qquad (2)$$

$$N = N_{elastic} + \delta N_{plastic}. \qquad (3)$$

If we do not consider the pure plastic effects, the plastic contribution vanishes and the ratio of $\tau_{elastic}$ and $N_{elastic}$ describes the usual (non-linear) friction behaviors that occur during the complete frictional cycle: Pre-Sliding (increase of friction coefficient when there is no-apparent or residual displacement), Gross-Sliding (observable displacement and decrease of friction coefficient) and Healing (friction coefficient recovery) (e.g., Parlitz et al., 2004, Marone and Saffer, 2015, Papangelo et al., 2015, and references therein).

Venegas-Aravena et al. (2019) state that the electrification within rocks is mainly due to a non-constant stress change during the semi brittle-plastic transition. This means that the temporal changes of the semi brittle-plastic stress ($\delta\sigma_{sbp}$) rules the total plastic stress ($\delta\sigma_{plastic}$). Thus, it implies that the plastic shear and normal stress can be written in terms of a linear combination of the temporal changes of $\delta\sigma_{sbp}$ as shown in Equations (4) and (5).

$$\delta\tau_{plastic} = k_1\delta\tau_{sbp} + k_2\delta^2\tau_{sbp} + o(\delta^2\tau) = k_1\,\dot{\tau}_{sbp}\delta t + k_2\,\ddot{\tau}_{sbp}(\delta t)^2 + o((\delta t)^2), \qquad (4)$$

$$\delta N_{plastic} = k_3\delta N_{sbp} + k_4\delta^2 N_{sbp} + o(\delta^2 N) = k_3\,\dot{N}_{sbp}\,\delta t + k_4\,\ddot{N}_{sbp}(\delta t)^2 + o((\delta t)^2), \qquad (5)$$

where $k_1,\ k_2,\ k_3$ and k_4 are dimensionless constants to be determined later, δt and $(\delta t)^2$ are the temporal variations from the first and second order time contribution, respectively. The temporal variations of the shear and normal semi brittle-plastic stress contributions are $\dot{\tau}_{sbp}, \ddot{\tau}_{sbp}, \dot{N}_{sbp}$ and $\ddot{N}_{sbp}$ respectively. The series expansions in Equations (4) and (5) are convenient and allow to write the plastic contribution as a sum of stresses that depend on time. This is relevant because the seismic-electromagnetic theory seeks to relate the temporal variable of the earthquake and the stress within the lithosphere. From now on, we refer to the semi brittle-plastic stress as the uniaxial stress σ.

It is possible to relate this shear, and the normal stresses from Equations (4) – (5) with the uniaxial stress using the geometry shown in Figure 1. In this Figure, we have a simple schematic representation of the lithosphere under uniaxial stress change $d\boldsymbol{\sigma}/dt$ in the presence of a fault with static friction coefficient μ and a dip angle of 30 degrees. We can write this uniaxial stress change in terms of the dip angle θ, normal and tangential direction (in red on Figure 1) of the fault, as shown in the following expression

$$\frac{d\boldsymbol{\sigma}}{dt} = \frac{d\sigma}{dt}(-\sin\theta\,\hat{N} + \cos\theta\,\hat{\tau}), \qquad (6)$$

where $d\sigma/dt$ corresponds to the magnitude of uniaxial temporal stress change. Using this expression, we write the brittle-plastic stress contributions in term of uniaxial stress change as:

$$\dot{N} = -\frac{d\sigma}{dt}\sin\theta. \qquad (7)$$

$$\dot{\tau} = \frac{d\sigma}{dt}\cos\theta. \qquad (8)$$

Replacing the Equations (2) – (8) in Equation (1), and considering a second-order linear combination, we obtain the static friction coefficient as a function of time, the fault angle and the semi brittle-plastics changes within lithosphere given by:

$$\mu(t) \approx \frac{\tau_0 + (k_1\,\dot{\sigma} + k_2\,\ddot{\sigma}\delta t)\cos\theta\,\delta t}{N_0 - (k_3\dot{\sigma} + k_4\,\ddot{\sigma}\,\delta t)\sin\theta\,\delta t}, \qquad (9)$$

where the dots above σ are the notation for the first and second temporal derivative of the uniaxial stress. According to Venegas-Aravena et al. (2019), the temporal stress change $\dot{\sigma}$ has approximately a sigmoidal shape, which can be written as $\dot{\sigma}(t) = a/(b + e^{(t0-t)*w})$, where a, b, w and t_0 are constants. In Figure 2 we represent $\dot{\sigma}$ and $\ddot{\sigma}$ as a function of time where we have used $a = b = w = 1$ and $t_0 = 10$ a.u.. According to De Santis et al. (2019b), most of the earthquakes recorded occurred close to the center of the Figure 2, which is when $t_{EQ} = t_0$. For instance, Marchetti and Akhoondzadeh (2018) have shown that the Mexico earthquake Mw8.2 occurred after this time ($t_{EQ} > t_0$). They also use daily values of magnetic anomalies ($B \propto \frac{d\sigma}{dt}$, which comes directly from the experimental equation: $I = \alpha_0 \frac{d\sigma}{dt}$, where I is the electric current and α_0 is a constant of proportionality (see Vallianatos, F. and Triantis and references therein)), thus $\delta t = 1\ day = 86400\ s$.

Let us now estimate the values of the constants of Equation (9). First, the dip or subduction angle θ, according to Maksymowicz (2015), this angle is close to 20 degrees at the depth ($\sim 30\ km$) and location (35°54′32″S, 72°43′59″W) of the Maule 2010 earthquake. Maksymowicz (2015) claimed that the static friction coefficient in the Chilean convergent margin is close $\mu_{ch} \approx 0.5$. Lamb (2006) calculated that the initial value of τ_0 is 15.4 MPa (constant) in southern Chile. Using μ_{ch}, it is expected that N_0 should be approximately equal to 30.8 MPa (constant).

In addition, rock experiments show that the values of $\dot{\sigma}$ are close to 1 MPa/s (e. g. Saltas et al., (2018)). This implies that $|k_1|$ and $|k_3|$ must be close to $\sim 10^{-4}$, in order to balance the δt factor. The values of k_2 and k_4 must be equal or lesser than $\sim 10^{-9}$,otherwise the values of the friction coefficient would be greater than 1. If we consider an initial increase of the normal stress, the sign of the constants should be negative for k_3, k_4 and positive for k_1, k_2. In Figure 3 we can see how the friction coefficient changes in time, when using values of k_1 and k_3 described above, and different values of k_2 and k_4 (second order contribution). When we use values of k_2 and k_4 of the order of $\sim 10^{-9}$, it is possible to observe how the friction decreases after the earthquake. Furthermore, it is important to note that the earthquake does not occur when the friction has its maximum value, but occurs close to the maximum. When we use values of k_2 and k_4 similar or lesser than $\sim 10^{-10}$ the contribution of $\ddot{\sigma}$ in Equation (9) vanishes.

Another critical point is related to the differential time. For instance, when we consider $\delta t \leq 1\ s$, the semi brittle-plastic stress term vanishes and the usual friction is recovered. This fact is especially relevant because the semi brittle-plastic contribution to the friction coefficient seems to be relevant only during large time scales. To summarize, the friction coefficient of Equation (9) could be seen as a generalization of the standard friction coefficient when large time scales are considered.

3. - Spatial distribution of stress changes and friction

In the previous section we have linked the friction coefficient to the semi brittle-plastic regime that generates microcracks and electrification within the rocks. An important caveat is that this phenomenon does not occur everywhere. For instance, Dobrovolsky et al. (1979) described a specific "preparation zone" required close to the future hypocenter in order to accumulate sufficient stress to trigger the earthquake. This criterion has been widely used by researchers to establish a threshold for determining where the magnetic measurements can be associated to earthquakes (e.g. De Santis et al., 2019a, De Santis et al., 2019b). In other words, the phenomenon is local. However, if this is applied, a variation of the friction coefficient related to the rock electrification phenomenon close to the fault would be expected, while a friction variation outside the zones of semi brittle-plastic influence would not.

In order to consider the local variations, we add to our model a separable spatial function to the uniaxial stress as given by $\bar{\sigma}(x,t) = \gamma(x)\sigma(t)$ (for simplicity we choose a uniaxial dependence). Where $\sigma(t)$ correspond to the same time function as considered in section 2 and $\gamma(x)$ is the dimensionless spatial distribution parallel to the fault (see the coordinate system in Figure 4). Let us mention that the values of $\gamma(x)$ are different when constant and non-constant stress changes are considered. With this in mind, we can re-write Equation (9) as:

$$\bar{\mu}\,(x,t) \approx \frac{\tau_0 + \gamma(k_1\,\dot{\sigma} + k_2\,\ddot{\sigma}\delta t\,)\cos\theta\,\delta t}{N_0 - \gamma(k_3\dot{\sigma} + k_4\,\ddot{\sigma}\,\delta t)\sin\theta\,\delta t}. \qquad (10)$$

After straightforward derivations, we get that the gradient of the friction coefficient along the fault using Equation (10) is given by:

$$\nabla\bar{\mu}(x,t) = \gamma'\,\frac{AN_0 + B\tau_0}{(N_0 - \gamma B)^2} = \gamma'\frac{\alpha\,\dot{\sigma}\delta t + \beta\,\ddot{\sigma}\delta t^2}{(N_0 - \gamma B)^2}, \qquad (11)$$

where $A = (k_1\,\dot{\sigma} + k_2\,\ddot{\sigma}\delta t\,)\cos\theta\,\delta t$, $B = (k_3\dot{\sigma} + k_4\,\ddot{\sigma}\,\delta t)\sin\theta\,\delta t$, $\alpha = N_0k_1\cos\theta + \tau_0k_3\sin\theta$ and $\beta = N_0k_2\cos\theta + \tau_0k_4\sin\theta$. Equation (10) and (11) imply that if we distribute the constant and non-constant temporal stress change in a non-uniform manner along the fault, then, it could be said that this phenomenon is local. This can be understood using the example of Figure 4: The Figure 4a shows a blue area of length L where we have a non-constant temporal stress change. There one observes a change in the friction coefficient inside the projected gray area (Figure 4b). Conversely, outside the area of length L (Figure 4c), we assume a constant stress change then there is no change in the friction coefficient (Figure 4d). Let us remind that the entire fault suffered from stress accumulation during the entire process. However, only the grey area is directly affected by the friction change. This shows that the temporal friction changes are restricted only to a specific area (grey area) on the fault. Hence, one observes non-zero friction coefficient gradient on the fault and we have a local phenomenon ($\nabla\,\bar{\mu} \neq 0 \Leftrightarrow Local$).

The process described in Figure 4 reveals why the magnetic measurements are not global. It also validates the locality criteria in terms of fault properties. Furthermore, the spatial distribution of magnetic field measurements is expected to have a length scale comparable to the friction coefficient change due to the dependency of $\gamma(x)$ in Equation (10). That is, the larger the detection area of magnetic anomalies, the larger the area where fault friction is changing. In addition, Venegas-Aravena et al. (2019) described how the uniaxial stress change implies a change in the b-value of the Gutenberg-Richter Law. It also implies that a significant earthquake is needed in order to satisfy this change in the Gutenberg-Richter Law. Therefore, a greater expected magnitude could be related to changes in the coefficient of friction within an area within the fault. However, changes in the friction coefficient do not directly imply the earthquakes generation itself.

4. - Stress drop and total friction coefficient: Spatial-temporal behavior

Up to this point, no changes in the elastic stresses have been considered in Equation (10). This section focuses on one of the elastic parameter that is involved in the seismic rupture process: the stress drop $\Delta\tau$. This parameter is one of the most relevant because it shows the shear stress differences prior and after the onset of the earthquake within the fault rupture area (e.g. Aki, 1966). Furthermore, this parameter is also related to the seismic waves radiated (through the corner frequency of waves) and the seismic moment M_0 (e.g. Eshelby, 1957, Brune, 1970, Baltay et al., 2011, and references therein). If we consider a circular

rupture area with radius d_{crack}, the stress drop $\Delta\tau$ is linked with the seismic moment M_0 through the following equation (Eshelby, 1957).

$$\Delta\tau = \frac{7}{16}\frac{M_0}{d_{crack}^3}. \qquad (12)$$

On the other hand, the seismic moment M_0 and the moment magnitude Mw in terms of the co-seismic magnetic field are also related. Hence, the seismic moment is given by:

$$M_0 \approx \mu_{sm}\frac{B_{cs}r^2}{\mu_m J}\frac{(3-D)}{D(D-2)}\left(l_{min}^{2-D}\right)\left(l_{max}^{D-3}\right)d, \qquad (13)$$

where μ_{sm} is the shear modulus, d the average slip, D fractal dimension of rock, B_{cs} the co-seismic magnetic field, J corresponds to the total electric current density, μ_m is the magnetic permeability of the medium, r the distance to the fault, l_{max} and l_{min} are the radius of the circular rupture area and the smallest microcrack length, respectively. The circular rupture is calculated using $l_{max} = \sqrt{S/\pi}$, where S corresponds to the total rupture area.

In this case, the rupture geometry is circular in both formulations, thus, $d_{crack} = l_{max}$. Replacing this into Equation (13) and Equation (12) we obtain:

$$\Delta\tau \approx \frac{7}{16}\,\mu_{sm}\frac{B_{cs}r^2}{\mu_m J}\frac{(3-D)}{D(D-2)}\left(l_{min}^{2-D}\right)\left(l_{max}^{D-6}\right)d. \qquad (14)$$

Equation (14) relates the stress drop with the co-seismic magnetic field, seismic rupture, and the electrical and mechanical properties of rocks (lithosphere). We can use the data from the Maule earthquake in order to compare the result of Equation (14) with those found by other researchers. If we use the fault values: $\mu_{sm} = 3.3 \times 10^{10}\ Pa$, $d = 4\ m$ and $S = 450 \times 120\ \text{km}^2$ (Vigny et al., 2011; Yue et al., 2014), the granite rock and brittle properties: $\mu_m = 13.5 \times 10^{-7}\ NA^{-2}$ (Scott, 1983), $J = 5 \times 10^{-6}\ Am^{-2}$ (Tzanis and Vallianatos, 2002), $l_{min} = 10^{-3}\ m$ (Shah, 2011) and $D = 2.6$ (Turcotte, 1997). The magnetic data $B_{cs} \approx 0.1\ nT$ at $r \approx 250$ km (Figure 5 in Venegas-Aravena et al. (2019)), we obtain a stress drop $\Delta\tau \approx 3.4\ MPa$. This result is in close agreement with the result of Luttrell et al. (2011) (4 MPa). Using this value, we can calculate the elastic shear stress as:

$$\tau_{elastic} = \tau_0 - \gamma_2\Delta\tau H(t - t_0), \qquad (15)$$

where $H(t - t_0)$ correspond to the step function centered at t_0 (the moment of the earthquake occurrence) and γ_2 is a dimensionless second step function that represents the fault area where the stress drop exists. This means that $\gamma_2 = 0$ outside the rupture area, and $\gamma_2 = 1$ if the point is within the rupture area. Combining this result into Equation (10), we calculate the total friction coefficient $\bar{\mu}_T$ of the fault as:

$$\bar{\mu}_T\,(x,t) \approx \frac{\tau_0 - \gamma_2\Delta\tau H(t-t_0) + \gamma\,(k_1\,\dot{\sigma} + k_2\,\ddot{\sigma}\delta t\,)\cos\theta\,\delta t}{N_0 - \gamma\,(k_3\dot{\sigma} + k_4\,\ddot{\sigma}\,\delta t)\sin\theta\,\delta t}. \qquad (16)$$

This total friction coefficient $\bar{\mu}_T$ is especially relevant because of the dependence of the co-seismic magnetic field B_{cs} (through the stress drop $\Delta\tau$) and the magnetic anomalies (through the relation $B \propto \dot{\sigma}$). Furthermore, Equation (16) explains the spatial distribution of friction along the fault in addition to their time variations. In Equation (16), the spatial changes of friction (represented by γ) are not necessarily related to the seismic rupture area (represented by γ_2). However, in the case when they are related, one expects that γ_2 is a function of γ. That is $\gamma_2 = \gamma_2(\gamma(x))$. In the general case the total friction coefficient gradient can be written as:

$$\nabla\bar{\mu}_T = \nabla\bar{\mu} + \Delta\tau H(t - t_0)\,\Gamma(\gamma, \gamma_2), \qquad (17)$$

where $\Gamma(\gamma,\gamma_2) = \frac{1}{(N_0-\gamma B)^2}\,[\gamma_2'(\gamma B - N_0) - \gamma'\gamma_2 B]$, $\nabla\bar{\mu}$ is the friction gradient already defined in Equation (11), and the same definition for A and B are used. The second term of Equation (17) implies that a more complex spatial friction distribution on the fault is expected after the earthquake. When no brittle-plastic contribution is considered ($\gamma = 0$), the friction is only proportional to the gradient of fault rupture distribution ($\nabla\bar{\mu}_T = -\Delta\tau H(t-t_0)\gamma_2'/N_0$). When $\gamma_2 \approx \gamma$, the two terms of the Total Friction Coefficient will be proportional to the spatial distribution gradient ($\nabla\bar{\mu}_T \propto \gamma'$). If the earthquake does not occur, the second term vanishes and Equation (11) is recovered.

As an illustration, if we consider one point affected by the rupture area, and the same values as in Figure 3, we can calculate the shape of the total friction coefficient as shown in Figure 5. The three cases show an increase of the friction coefficient prior to the earthquake, and in the three cases the friction reaches its maximum values before the earthquake (at t=10 a.u.). The subsequent decrease is due to the stress drop influence calculated using the co-seismic magnetic field B_{cs}. After the earthquake, in none of the cases, the friction is completely recovered to its values before the earthquake.

As a second illustration, it is also possible to compare the temporal behavior of the friction coefficient at different points within the fault. For instance, in Figure 6 (top) we show the different friction behaviors expected if we consider the Total friction coefficient. The red area indicates the area where the friction drop occurs. A friction drop is not expected to occur outside the red zone. However, it is possible to observe differences in the coefficient of friction close to the rupture zone where $\gamma_2 \neq \gamma$ (yellow area). Both in the rupture zone and its surroundings (marked as red and yellow areas respectively in Fig.6) show changes in the coefficient of friction prior to the rupture. In stark contrast, the standard friction drop is expected only in the rupture zone (red area) and a non-measurable change in friction is expected prior to the earthquake (Figure 6 bottom).

We can summarize our analysis by using two different distributions of γ and γ_2. For instance, in Figure 7 we show the double-sigmoidal distribution for γ and γ_2(black and red curves respectively) along the fault x-direction (of total length $2x_{half}$). The dimensionless distribution is defined as a combination of sigmoidal function used in the section 2 as:

$$\gamma(x),\gamma_2(x) = \begin{cases} \dfrac{a}{b - e^{(x_0 - x)*w}}, & x < x_{half} \\ 1 - \dfrac{a}{b - e^{(x_0 + L - x)*w}}, & x \geq x_{half} \end{cases}. \qquad (18)$$

If we consider $a = b = 1$ and $x_{half} = 10$ a.u. in both distributions, and $x_0 = 5$ a.u. , $L = 10$ a.u. and $w = 1$ a.u. for γ and $x_0 = 8$ a.u. , $L = 4$ a.u. and $w = 10$ a.u. for γ_2, we get the two distributions of Figure 7. These values indicate the same situation as discussed in Figure 6. That is a rupture length ($L = 4$ a.u. in γ_2 represents the x-direction of the red area in Figure 6) lesser than the friction coefficient influenced by semi brittle-plastic stress (here $L = 10$ a.u. in γ represent the x-direction of the yellow area in Figure 6). Using both sets of values, those used in the stress drop (Equation (14)) and also the same k-parameters used in Equation (9), we calculate the total friction coefficient (Equation (16)) as shown in Figure 8 (case $k_2 = k_4 = 10^{-9}$). At time t = 0 a.u., no friction changes occur ($\bar{\mu}_T = 0.5$). However, the friction increases at t=5 a.u., where the spatial distribution γ is initially defined as non-zero ($x \in [5, 15]$ a.u.). The friction increases up to t=10, a.u. the time corresponding to the earthquake occurrence. The earthquake rupture length is shown as a sudden friction decrease ($x \in [8, 12]$ a.u.) from 0.76 to 0.67. In the zone immediately close to the rupture, the friction increases even more up to the maximum values (0.77), while the rupture section decreases the friction. After this time (t~12 a.u.), the rupture and the surrounding section experience a friction decrease.

The case of $k_2 = k_4 = 10^{-10}$ is shown in Figure 9. The rupture is shown as a blue area at t=10 a.u. in section $x \in [8, 12]$ a.u.. At this time and location, we observe that the friction decreases to similar initial values (~0.5). The friction of this rupture section increases after the earthquake up to ~0.6. On the other hand, the rupture's surrounding section increases up to the maximum values (~0.7). Despite those facts, the initial (t=0 a.u.) and final (t=20 a.u.) friction values are almost identical for both cases. For instance, the rupture area has values close to 0.6 in Figures 8 and 9. The surrounding rupture section has values close to 0.69 in both cases and the section away from the rupture (close to x=0 a.u. and x=20 a.u.) always has the same initial value (0.5) in both cases. However, both cases exhibit a complex time behavior after the earthquake occurrence, as Equation (17) indicates.

Finally when the semi brittle-plastic contribution is not considered, we get that $\gamma = 0$. The result is shown in Figure 10 and is only observed when the sudden friction decrease at t=10 a.u. (and $x \in [8, 12]$ a.u.). In this later case none of the other complex friction behavior is observed.

5. - The semi brittle-plastic Gutenberg-Richter law

A general expression for friction has been obtained in Equation (16). Following this we can adapt the Gutenberg-Richter's law in this semi brittle-plastic context. Let us remind that this law establishes a relation between the number of earthquakes in a region and the magnitude of them (Gutenberg and Richter, 1944). Mathematically, this link is written as: $\log N = a - b \times m$. Where N is the number of earthquakes with magnitude equal to or greater than m, and a and b are constants. However, the b-value of this law might evolve in time. Indeed, De Santis et al. (2011) determined an equation that relates the temporal evolution of the parameter b ($b = b(t)$) and the measure of the entropy (stress) $H(t)$ of that region as $b(t) = b_{max} 10^{-H(t)}$, where $b_{max} = e \log_{10} e$. The entropy $H(t)$ is assumed to be proportional to the real stress in the lithosphere (Venegas-Aravena et al., 2019). If we consider the total shear stress τ_T in the fault described by Equation (16), we can write:

$$b(t) = b_{max} 10^{-k_0 \tau_T}, \qquad (19)$$

where $\tau_T = \tau_0 - \gamma_2 \Delta\tau H(t - t_0) + \gamma (k_1 \dot{\sigma} + k_2 \ddot{\sigma} \delta t) \cos\theta \, \delta t$ and k_0 is a constant with dimension of an inverse stress. If we use the same values as in Figure 5 ($k_2 = k_4 = 10^{-9}$), we get the temporal evolution of the b-value (Figure 11a). Figure 11a shows a decrease in the b-value until the earthquake occurs (at t=10 a.u.). Figure 11b shows the Gutenberg-Richter's law at three instants of time (and $k_0 = 0.01$, a=1): initial (t=0 a.u.), prior to the earthquake (t=9 a.u.) and final (t=20 a.u.). This Figure shows how large earthquakes (Mw ~ 6) are not expected at the initial moment (blue line). However, just before the earthquake, an M8-class earthquake should be expected (green line). After the earthquake one would only expect earthquakes no greater than Mw ~ 7 to exist (red line). Figure 12a and 12b show the same previous case but now considering $k_2 = k_4 = 10^{-10}$. In this case there is no difference between time, immediately before the earthquake (t=9 a.u.) and at the final time (t=20 a.u.). In addition, using these parameters ($k_2 = k_4 = 10^{-10}$), smaller magnitudes are reached than using $k_2 = k_4 = 10^{-9}$ (Mw~7 and Mw~8 respectively). This is why it is more likely to find earthquakes of greater magnitude when considering the contribution of the $\ddot{\sigma}$ term in the analysis.

6. - Rupture time t_0

In section 5 we determine that $k_2 = k_4 = 10^{-9}$ were the most adequate values. Despite this fact, the Gutenberg-Richter law does not provide an approximate time $\boldsymbol{t_0}$ for the earthquake occurrences. If we

look at Equation (16), the term $\boldsymbol{t_0}$ appears explicitly (in the step function). However, $\boldsymbol{t_0}$ appears only after the earthquake, so it is not possible to find $\boldsymbol{t_0}$ analytically before the rupture (using the rupture itself). This means that we must find an estimate using the other parameters. One way to do it is to consider the differential total friction coefficient $d\bar{\mu}_T$ to find an approximate rupture time t_0. Figure 13 shows $d\bar{\mu}_T$ considering $\gamma_2 = \gamma = 1$, $k_2 = k_4 = 10^{-9}$ and $k_2 = k_4 = 10^{-10}$. When major earthquakes ($k_2 = k_4 = 10^{-9}$) are considered, the rupture occurs after the maximum value ($(d\bar{\mu}_T)_{MAX}$), when $d\bar{\mu}_T \approx \frac{1}{2}\,(d\bar{\mu}_T)_{MAX}$ (Figure 13 up). When $k_2, k_4 = 10^{-10}$, the rupture also occurs after the maximum value, in this case $d\bar{\mu}_T \approx 0.9\,(d\bar{\mu}_T)_{MAX}$ (Figure 13 down). Considering these two limiting cases in this framework we conclude that earthquakes occur after $(d\bar{\mu}_T)_{MAX}$ when the differential total friction coefficient decrease to $d\bar{\mu}_T \approx \mathrm{C}\,(d\bar{\mu}_T)_{MAX}$, where $C \in [0.5,\ 0.9]$.

The time between $d\bar{\mu}_T \approx (d\bar{\mu}_T)_{MAX}$ and $d\bar{\mu}_T \approx \mathrm{C}\,(d\bar{\mu}_T)_{MAX}$ can be denoted by δ. This δ parameter increases when C decreases and viceversa, so δ is inversely proportional to C ($\delta \propto C^{-1}$). Then, we arrive at an expression for the general rupture time t_0 as follows:

$$t_0 \approx t_{\mathrm{C}\,(d\bar{\mu}_T)_{MAX}} = t_{(d\bar{\mu}_T)_{MAX}} + \delta, \quad t > t_{(d\bar{\mu}_T)_{MAX}}\,, \qquad (20)$$

where $t_{(d\bar{\mu}_T)_{MAX}}$ is the time when $d\bar{\mu}_T \approx (d\bar{\mu}_T)_{MAX}$. Note that the Equation (20) is only valid after the maximum value $(d\bar{\mu}_T)_{MAX}$ is reached. Equation (20) is general, however, considering the Gutenberg-Richter law, we expect that C values close to 0.5 are necessary to represent earthquakes of greater magnitude in this theoretical framework.

7. - Discussion and conclusions

In this work we have linked key parameters associated with the geological fault with magnetic measurements. Both stress drops and the semi brittle-plastic stress were linked to friction coefficient (on the fault) equation in terms of magnetic measurements (Equation (16)). One of the main points of Equation (16) corresponds to the fact that the Total Friction Coefficient $\bar{\mu}_T(x,t)$ is entirely determined by the spatial distribution of the non-constant stress changes within the lithosphere. If the Seismo-electromagnetic theory is applied, it means that the rupture process is controlled by the non-constant stress changes that surround the fault and not by the fault itself. In this scenario, the earthquakes might occur at places on the fault that are being affected by a continuous friction increase prior to rupture (this friction increase occur regardless of the values of k_2 and k_4 used in the analysis). In our work we have shown that the Total Friction Coefficient depends on two different spatial distributions. The first one is associated with the uniaxial stress changes $\gamma(x)$ and the second one to the rupture area $\gamma_2(x)$. These two distributions are not necessarily correlated. In the case where they are comparable (that is: $|\gamma(x) - \gamma_2(x)| \approx 0$), it means that the lithosphere area affected by non-constant uniaxial stress changes is a determining factor for predicting the earthquake magnitude and location before it occurs. This is $\gamma(x) \approx \gamma_2(x) \approx 0$ if x belong to sections where $\dot{\sigma} = cte$ and $\gamma(x), \gamma_2(x) \neq 0$ if $x \in L$, where L is the rupture length (at places where $\dot{\sigma} \neq cte$). The seismic moment M_0 is proportional to this length L (Aki, 1966), and the seismic moment magnitude M_w depends on the seismic moment (Hanks and Kanamori, 1979), implying that the seismic moment magnitude depends on the spatial distribution of the total friction coefficient variations. As the non-constant uniaxial stress changes also could create magnetic signals due the microcracks of rocks (Venegas-Aravena et al., 2019, and references therein), it is reasonable to affirm that larger area of magnetic anomalies could imply a larger earthquake. This is the locality (or Dobrovolsky) criteria used by some researchers when they relate some electromagnetic measurements to earthquakes (e.g., De Santis et al., 2019a, and references therein). If in this case we also consider the initial time of friction increase (impending rupture time), the approximate magnitude, the approximate location and the approximate imminent time could be theoretically determined through Equation xxxx.

For the limiting case when $|\gamma(x) - \gamma_2(x)| \gg 0$ we have seen that the locality criteria do not hold anymore. Hence, the earthquakes occurrences cannot be related to the non-constant stress changes and the magnetic field. This limiting case forbids the possibility of a real earthquake prediction using this simple theoretical base. This later case may also imply that the cumulative stress on the fault is not enough to generate a seismic rupture at any point on the fault (this is $\gamma_2(x) = 0$). This means that the accumulated elastic energy that is injected into the fault is not sufficient to spread the rupture (the last energy is called Fracture Energy G_C, see Ohnaka, 2013 and Nielsen et al., 2016). This scenario could indicates that the stress changes in the semi brittle-plastic regime is not a sufficient condition to the earthquake generation, however, it could be a necessary condition.

With respect to the size of earthquakes in the present model, the section 5 has shown that earthquakes have greater magnitudes when $k_2 = k_4 \approx 10^{-9}$. If we consider those values in Figure 5, we see that the total friction coefficient is also higher. This is ~0.75 when $k_2 = k_4 \approx 10^{-9}$ and sensibly larger than ~0.6 when $k_2 = k_4 \approx 10^{-10}$. This indicates that there is a correlation between the size of the earthquake and the total friction coefficient. Hence, the earthquake has a greater magnitude when there is a higher total friction coefficient (or shear stress τ). This means that $\gamma_2 = \gamma_2(\bar{\mu}_T)$, therefore, the rupture length L of Equation (18) is proportional to $\bar{\mu}_T$ (that is: $L = \alpha\bar{\mu}_T(t_0)$). Note that this is independent of the value of $|\gamma(x) - \gamma_2(x)|$, since it comes directly from the Gutenberg-Richter's law. However, in this case $\bar{\mu}_T$ is homogeneous, so more studies will be needed in order to determine L.

Finally, this theoretical work has provided a possible mechanism that explains several magnetic measurements performed recently. This work provides equally some necessary conditions of the fault in order to trigger earthquakes in terms of their magnetic properties. We think that future researches of the LAIC effect community should focus on the lithospheric-fault dynamics as one of the promising topics. When the lithosphere part of this effect would be better understood, the other effects will have a stronger theoretical basis that will help in order to perform measurements and/or accurate predictions.

Acknowledgments

In memory of Marcela Larenas Clerc (1960-2019). P.V.-A. acknowledges Patricia Aravena, Alejandro Venegas, Patricia Venegas and Richard Sandoval for outstanding support to carry out this work, and Valeria Becerra-Carreño for her scientific support. D. L. acknowledges partial financial support from Centers of excellence with BASAL/CONICYT financing, grant FB0807, CEDENNA.

References

Aki, K.: Generation and propagation of G waves from the Niigata earthquake of June 14, 1964. Part 2. Estimation of earthquake moment, released energy and stress-strain drop from G wave spectrum. Bulletin of the Earthquake Research Institute, 44: 73–88, 1966.

Anastasiadis, C., Triantis, D., Stavrakas, I. and Vallianatos, F.: Pressure Stimulated Currents (PSC) in marble samples. Ann. Geophys., 47, 1, pp. 21-28, 2004.

Baltay, A., Ide, S., Prieto, G. and Beroza, G.: Variability in earthquake stress drop and apparent stress. Geophysical Research Letters. VOL. 38, L06303, doi:10.1029/2011GL046698, 2011.

Brune, J. N.: Tectonic stress and the spectra of seismic shear waves from earthquakes, J. Geophys. Res., 75(26), 4997–5009, doi:10.1029/JB075i026p04997, 1970.

Byerlee, J.D.: Friction of Rocks. Pure and Applied Geophysics. 116 (4–5): 615–626. doi:10.1007/BF00876528, 1978.

Chen, G.S.: Fundamentals of contact mechanics and friction. Handbook of Friction-Vibration Interactions, 71–152. doi:10.1533/9780857094599.71, 2014.

Cordaro, E.G., Venegas, P. and Laroze, D.: Latitudinal variation rate of geomagnetic cutoff rigidity in the active Chilean convergent margin. Ann. Geophys., 36, 275–285, https://doi.org/10.5194/angeo-36-275-2018, 2018.

De Santis, A., Cianchini, G., Favali, P., Beranzoli, L., and Boschi, E.: The Gutenberg–Richter Law and Entropy of Earthquakes: Two Case Studies in Central Italy, B. Seismol. Soc. Am., 101, 1386–1395, https://doi.org/10.1785/0120090390, 2011.

De Santis, A., Balasis, G., Pavón-Carrasco, F.J., Cianchini, G. and Mandea, M.; Potential earthquake precursory pattern from space: The 2015 Nepal event as seen by magnetic Swarm satellites. Earth and Planetary Science Letters 461, 119–126, http://dx.doi.org/10.1016/j.epsl.2016.12.037, 2017.

De Santis, A., Abbattista, C., Alfonsi, L., Amoruso, L., Campuzano, S.A., Carbone, M., Cesaroni, C., Cianchini, G., De Franceschi, G., De Santis, A., Di Giovambattista, R., Marchetti, D., Martino, L., Perrone, L., Piscini, A., Rainone, M.L., Soldani, M., Spogli, L. and Santoro, F.: Geosystemics View of Earthquakes, Entropy2019,21, 412; doi:10.3390/e21040412, 2019a.

De Santis, A.; Marchetti, D.; Spogli, L.; Cianchini, G.; Pavón-Carrasco, F.J.; Franceschi, G.D.; Di Giovambattista, R.; Perrone, L.; Qamili, E.; Cesaroni, C.; De Santis, A.; Ippolito, A.; Piscini, A.; Campuzano, S.A.; Sabbagh, D.; Amoruso, L.; Carbone, M.; Santoro, F.; Abbattista, C.; Drimaco, D.:

Magnetic Field and Electron Density Data Analysis from Swarm Satellites Searching for Ionospheric Effects by Great Earthquakes: 12 Case Studies from 2014 to 2016. Atmosphere 2019, 10, 371, 2019b.

Dobrovolsky I.R., Zubkov S.I. and Myachkin V.I..: Estimation of the size of earthquake preparation zones. Pure Appl. Geophys. Volume 117, Issue 5, pp1025–1044. doi:10.1007/BF00876083, 1979.

Eshelby, J. D.: The determination of the elastic field of an ellipsoidal inclusion, and related problems, Proc. R. Soc. Lond. A. Math. Phys. Sci., 376–396, doi:10.1098/rspa.1983.0054, 1957.

Freund, F.: Rocks That Crackle and Sparkle and Glow: Strange Pre-Earthquake Phenomena. Journal of Scientic Exploration, Vol. 17, No. 1, pp. 37–71, 2003.

Gutenberg, B. and Richter, C. F.: Frequency of earthquakes in California, B. Seismol. Soc. Am., 34, 185–188, 1944.

Hanks, T. C. and Kanamori, H.: A moment magnitude scale, J. Geophys. Res., 84, 2348–2350, https://doi.org/10.1029/JB084iB05p02348, 1979

Luttrell, K. M., Tong, X., Sandwell, D.T., Brooks, B.A. and Bevis, M.G.: Estimates of stress drop and crustal tectonic stress from the 27 February 2010 Maule, Chile, earthquake: Implications for fault strength, J. Geophys. Res., 116, B11401, doi:10.1029/2011JB008509, 2011.

Maksymowicz, A.: The geometry of the Chilean continental wedge: Tectonic segmentation of subduction processes off Chile. Tectonophysics 659 (2015) 183–196, doi: 10.1016/j.tecto.2015.08.007, 2015.

Marchetti, D. and Akhoondzadeh, M.: Analysis of Swarm satellites data showing seismo-ionospheric anomalies around the time of the strong Mexico (Mw = 8.2) earthquake of 08 September 2017. Advances in Space Research 62 (2018) 614–623, https://doi.org/10.1016/j.asr.2018.04.043, 2018.

Marone, C. J. and Saffer, D.M.: The Mechanics of Frictional Healing and Slip Instability During the Seismic Cycle, Treatise on Geophysics: Second Edition, 4 , pp. 111-138. DOI: 10.1016/B978-0-444-53802-4.00092-0, 2015.

Nielsen, S., Spagnuolo, E., Violay, M., Smith, S., Di Toro, G. and Bistacchi, A.: G: Fracture energy, friction and dissipation in earthquakes. J. Seismol. (2016) 20:1187–1205, DOI 10.1007/s10950-016-9560-1, 2016.

Ohnaka, M. (2013). In: The Physics of Rock Failure and Earthquakes. Cambridge: Cambridge University Press. doi:10.1017/CBO9781139342865.007, 2013.

Papangelo, A., Ciavarella, M. and Barber, J. R.: Fracture mechanics implications for apparent static friction coefficient in contact problems involving slip-weakening laws471Proc. R. Soc. A http://doi.org/10.1098/rspa.2015.0271, 2015.

Parlitz, U., Hornstein, A., Engster, D., Al-Bender, F., Lampaert, V., Tjahjowidodo, T., Fassois, S.D., Rizos, D., Wong, C.X., Worden, K. and Manson, G.: Identification of pre-sliding friction dynamics, Chaos 14, 420–430 (2004). https://doi.org/10.1063/1.1737818, 2004.

Potirakis, S.M., Contoyiannis, Y., Asano, T. and Hayakawa, M.: Intermittency-induced criticality in the lower ionosphere prior to the 2016 Kumamoto earthquakes as embedded in the VLF propagation data observed at multiple stations. Tectonophysics, 722, 422-431. 2018a.

Potirakis, S.M., Asano, T. and Hayakawa, M.: Criticality Analysis of the Lower Ionosphere Perturbations Prior to the 2016 Kumamoto (Japan) Earthquakes as Based on VLF Electromagnetic Wave Propagation Data Observed at Multiple Stations. Entropy 2018, 20, 199; doi: 10.3390/e20030199, 2018b.

Saltas V., Vallianatos F., Triantis D. and Stavrakas I.: Complexity in Laboratory Seismology. Complexity of Seismic Time Series, pages 239-273, 2018.

Scott, J.H.: Electrical and Magnetic properties of rock and soil. UNITED STATES DEPARTMENT OF THE INTERIOR GEOLOGICAL SURVEY. USGS Open-File Report 83-915, 1983.

Schekotov, A. and Hayakawa, M.: Seismo-meteo-electromagnetic phenomena observed during a 5-year interval around the 2011 Tohoku earthquake. Physics and Chemistry of the Earth, 85–86, 167-173, http://dx.doi.org/10.1016/j.pce.2015.01.010, 2015.

Shah, K. P.: The Hand Book on Mechanical Maintenance. Practical Maintenance. Compiled by: K P Shah. http://practicalmaintenance.net/?p=1135, 2011.

Sun, N. P., & Mosleh, M.: The Minimum Coefficient of Friction: What Is It? CIRP Annals, 43(1), 491–495. doi:10.1016/s0007-8506(07)62260-4, 1994.

Turcotte, D. L.: Fractals and Chaos in Geology and Geophysics, Cambridge University Press, Second edition, 397 p., 1997.

Tzanis A. and Vallianatos F.: A physical model of electrical earthquake precursors due to crack propagation and the motion of charged edge dislocations, in: Seismo Electromagnetics (Lithosphere–Atmosphere–Ionosphere-Coupling), TerraPub, 2002, pp. 117–130, 2002.

Utada, H., Shimizu, H., Ogawa, T., Maeda, T., Furumura, T., Yamamoto, T., Yamazaki, N., Yoshitake, Y. and Nagamachi, S.: Geomagnetic field changes in response to the 2011 off the Pacific Coast of Tohoku earthquake and tsunami, Earth Planet. Sci. Lett., 311, 11–27, doi:10.1016/j.epsl.2011.09.036, 2011.

Vallianatos, F. and Tzanis, A.: Electric Current Generation Associated with the Deformation Rate of a Solid: Preseismic and Coseismic Signals. Phys. Chem.Earth,Vol. 23, No. 9-10, pp. 933-938, 1998.

Vallianatos, F. and Tzanis, A.: On the nature, scaling and spectral properties of pre-seismic ULF signals. Natural Hazards and Earth System Sciences, 3: 237–242, European Geosciences Union, 2003.

Vallianatos, F. and Triantis, D.: Scaling in Pressure Stimulated Currents related with rock fracture, Physica A, 387, 4940–4946, https://doi.org/10.1016/j.physa.2008.03.028, 2008.

Venegas-Aravena, P., Cordaro, E. G., and Laroze, D.: A review and upgrade of the lithospheric dynamics in context of the seismo-electromagnetic theory, Nat. Hazards Earth Syst. Sci., 19, 1639–1651, https://doi.org/10.5194/nhess-19-1639-2019, 2019.

Vigny, C., Socquet, A., Peyrat, S., Ruegg, J.-C., Metois, M., Madariaga, R., Morvan, S.,Lancieri, M., Lacassin, R., Campos, J., Carrizo, D., Bejar-Pizarro, M., Barrientos, S.,Armijo, R., Aranda, C., Valderas-Bermejo, M.-C., Ortega, I., Bondoux, F., Baize, S.,Lyon-Caen, H., Pavez, A., Vilotte, J.P., Bevis, M., Brooks, B., Smalley, R., Parra, H.,Baez, J.-C., Blanco, M., Cimbaro, S. and Kendrick, E.: The 2010 Mw 8.8 Maule Megathrust Earthquake of Central Chile, monitored by GPS. Science 332,1417–1421, 2011.

Yue, H., Lay, T., Rivera, L., An, C., Vigny, C., Tong, X. and Báez Soto, J.C.: Localized fault slip to the trench in the 2010 Maule, Chile Mw = 8.8 earthquake from joint inversion of high-rate GPS, teleseismic body waves, InSAR, campaign GPS, and tsunami observations, J. Geophys. Res. Solid Earth, 119, 7786–7804, doi:10.1002/2014JB011340, 2014.

Captions Figures

Figure 1: Schematic description of the non-constant uniaxial stresses in presence of a fault with friction coefficient μ and dip angle θ.

Figure 2: Dimensionless representation of normalized first and second temporal change of the uniaxial stress used by Venegas-Aravena et al. (2019). According to De Santis et al. (2019a) the earthquakes occur close to the center of figures. Here it is when $t = t_0 = 10$ a.u..

Figure 3: Temporal behavior of the semi brittle-plastic friction coefficient using different parameters. In all the cases it's possible to observe an increase in the friction before earthquake (t = 10 a.u.). However, the friction decreases after the earthquake only if k_2 and k_4 has values of $\sim 10^{-9}$.

Figure 4: Schematic description of friction gradient on the fault. When a constant and non-constant temporal stress change is applied at different paces within the lithosphere, a non-zero friction coefficient gradient is expected.

Figure 5: Total fiction coefficient from the Seismo-electromagnetic Theory derivation. If we consider one point within the rupture area, the highest values of friction are found before the earthquake (t = 10 a.u.). The friction decreases at t=10 a.u. was calculated using the stress drop in function of the co-seismic magnetic field. The maximum value is not completely recovery after the earthquake occur.

Figure 6: Schematic comparison among different friction behaviors related with seismic rupture area. Above the result of friction in the context of The Seismo-electromagnetic Theory is presented. At the bottom the classical view of the friction. When the rupture occurs, de friction drop is observed in the two theories. However, exist a friction increase in the case studied in this work.

Figure 7: Spatial distribution of γ and γ_2. These functions represent the different sections (or behavior) of friction on the fault along x-direction. The distribution γ_2 represent the stress drop section and distribution γ represent the semi brittle-plastic influence region.

Figure 8: Spatial-temporal Total Friction Coefficient $\bar{\mu}_T(x,t)$ along fault x-direction using $k_2 = k_4 = 10^{-9}$, and the right color bar indicate the friction coefficient values at a certain time and position. The earthquake occurs when $t = 10$ a.u.. At this time, the stress drop (defined by the distribution γ_2) $\Delta\tau \in [8,12]$ a.u..

Figure 9: Same spatial-temporal Total Friction Coefficient, however, using $k_2, k_4 = 10^{-10}$.

Figure 10: Total Friction Coefficient using no semi brittle-plastic contribution. That is $\gamma(x) = 0, \forall x \in [0,2x_{half}]$. The friction variation exists only when the earthquake occurs ($t = 10$ a.u.) and at the earthquake rupture place ($\Delta\tau \in [8,12]$ a.u. in this case).

Figure 11: Above: The b-value using $\sigma = \alpha\,\tau$; $k_2 = k_4 = 10^{-9}$ and $\alpha = 0.01$. Bottom: The Gutenberg-Richter Law for instants time $t = 0$ a.u., $t = 9$ a.u. and $t = 20$ a.u.. The b-value decreases before the earthquake implying stronger seismic events.

Figure 12: The b-value and Gutenberg-Richter Law using $k_2 = k_4 = 10^{-10}$. The green and red curves are the same.

Figure 13: Different rupture's time viewed from the differential total friction coefficient $d\bar{\mu}_T$ and using different values of k_2 and k_4. The rupture occurs after the maximum differential total friction coefficient $(d\bar{\mu}_T)_{MAX}$, when $d\bar{\mu}_T$ have values close to 0.5-0.9 times $(d\bar{\mu}_T)_{MAX}$.

Figure 1

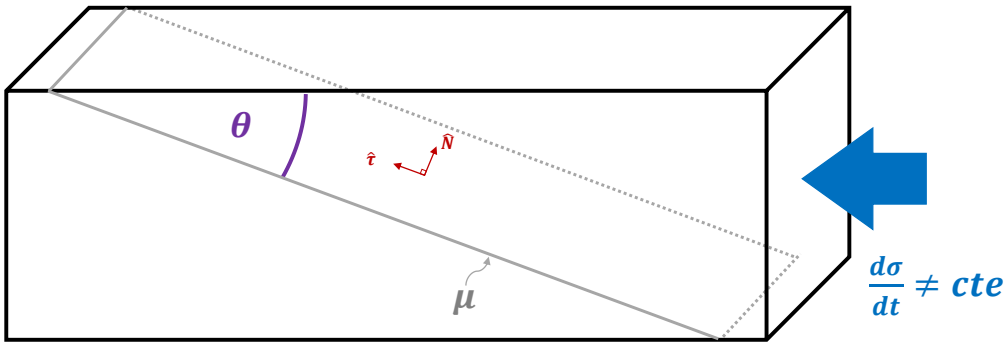

Figure 2

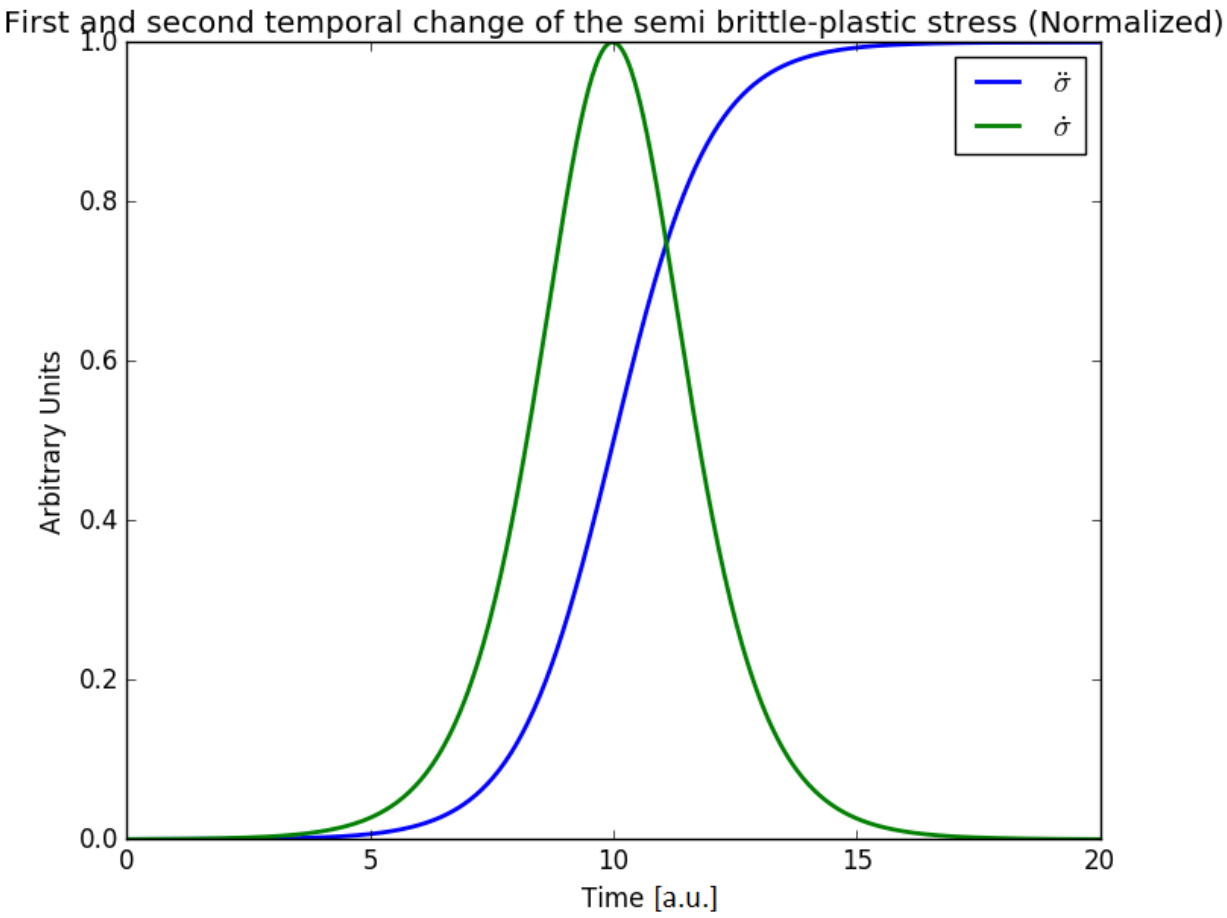
First and second temporal change of the semi brittle-plastic stress (Normalized)
Arbitrary Units
Time [a.u.]
0.0
0.2
0.4
0.6
0.8
1.0
0
5
10
15
20
$\ddot{\sigma}$
$\dot{\sigma}$

Figure 3

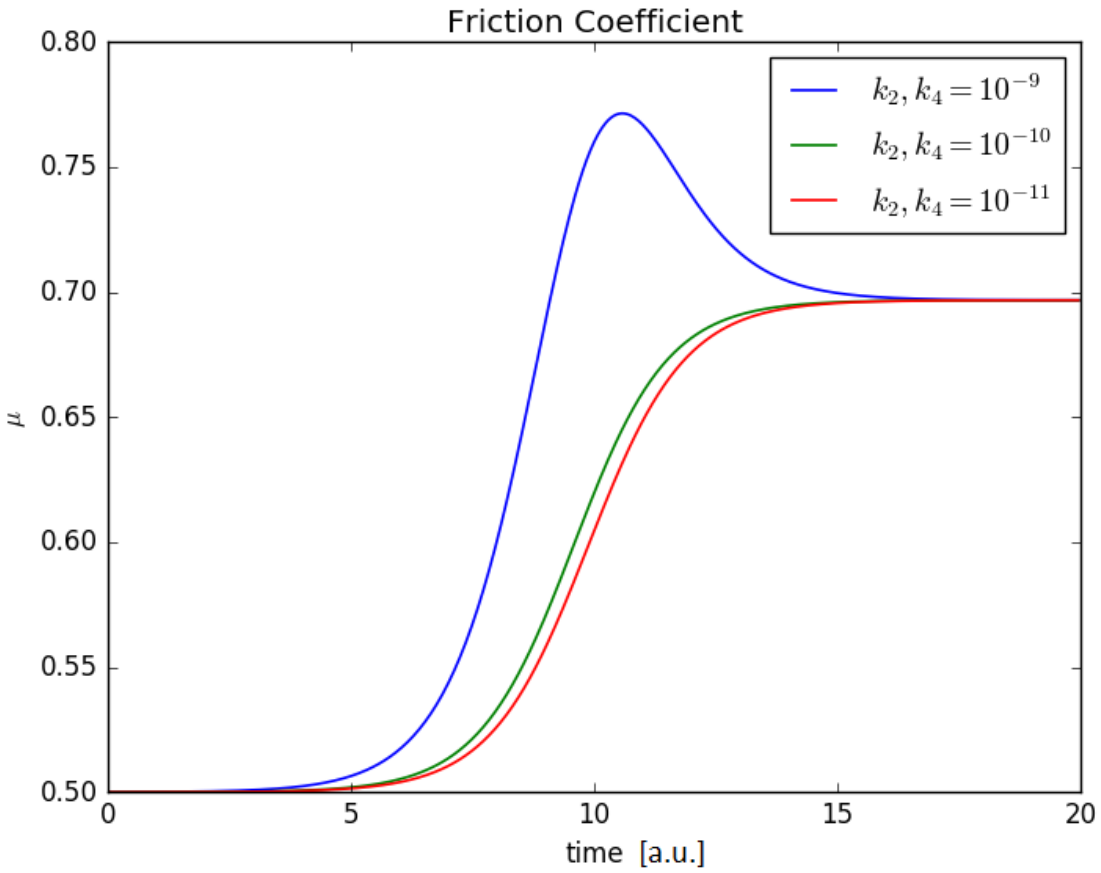
Friction Coefficient
0.80
0.75
0.70
0.65
0.60
0.55
0.50
μ
0
5
10
15
20
time [a.u.]
$k_2, k_4 = 10^{-9}$
$k_2, k_4 = 10^{-10}$
$k_2, k_4 = 10^{-11}$

Figure 4

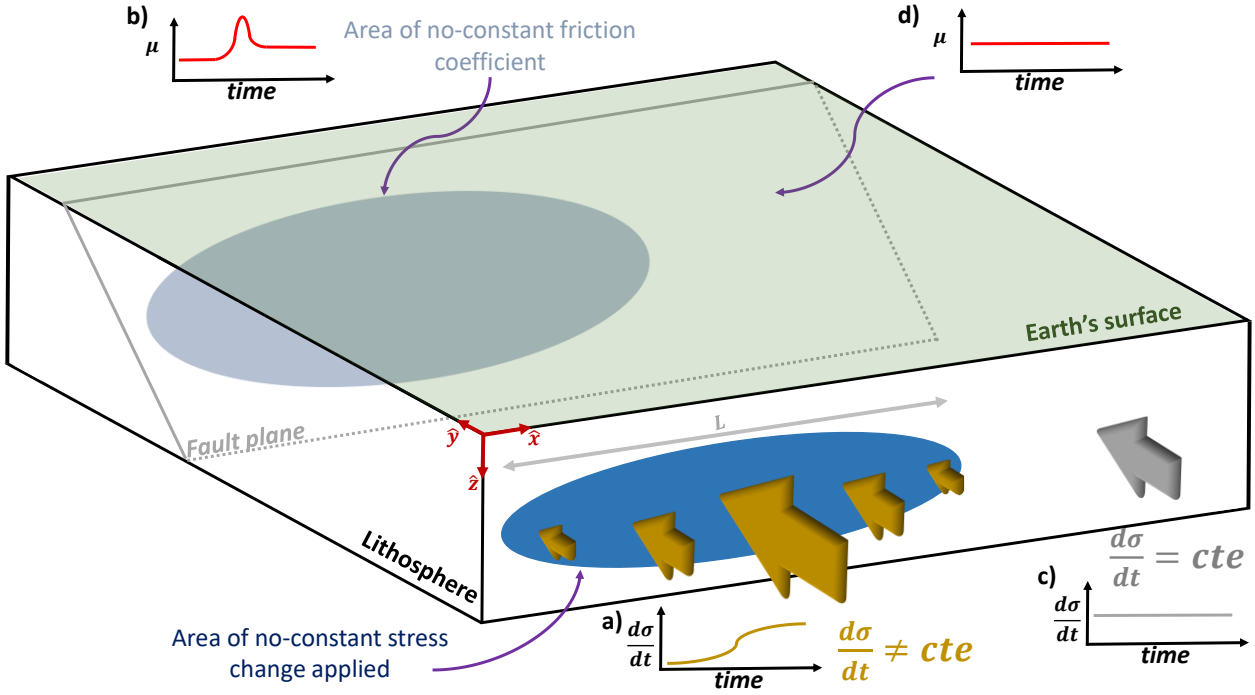
b)
μ
time
Area of no-constant friction coefficient
d)
μ
time
Earth's surface
Fault plane
L
Lithosphere
Area of no-constant stress change applied
a)
dσ/dt
time
dσ/dt ≠ cte
c)
dσ/dt = cte
dσ/dt
time

Figure 5

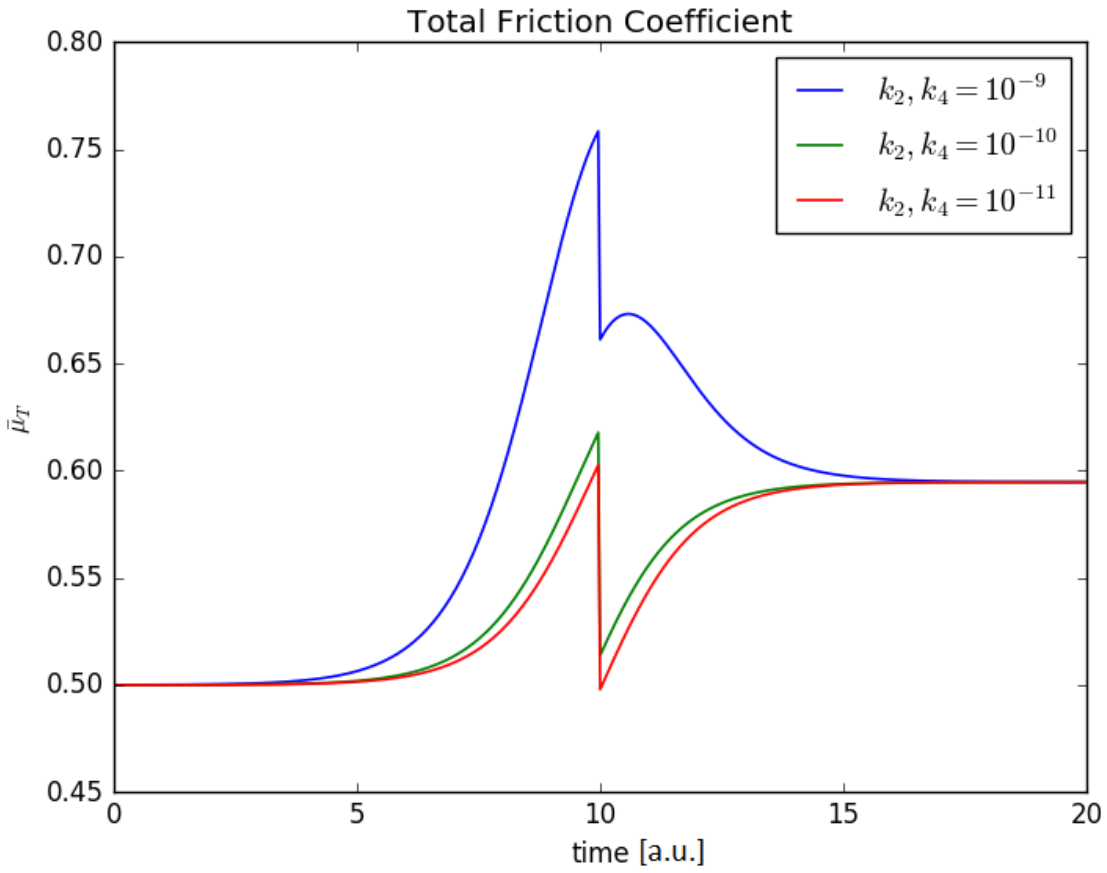
Total Friction Coefficient
$k_2, k_4 = 10^{-9}$
$k_2, k_4 = 10^{-10}$
$k_2, k_4 = 10^{-11}$
$\bar{\mu}_T$
0.80
0.75
0.70
0.65
0.60
0.55
0.50
0.45
0
5
10
15
20
time [a.u.]

Figure 6

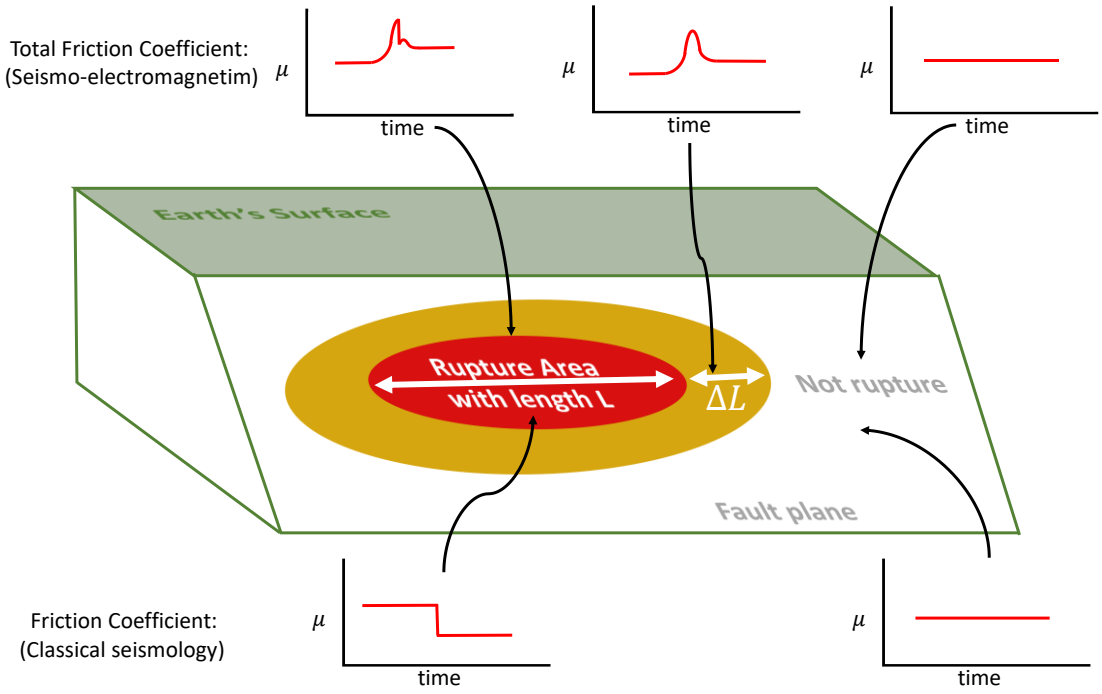
Total Friction Coefficient:
(Seismo-electromagnetim)
μ
time
μ
time
μ
time
Earth's Surface
Rupture Area
with length L
ΔL
Not rupture
Fault plane
Friction Coefficient:
(Classical seismology)
μ
time
μ
time

Figure 7

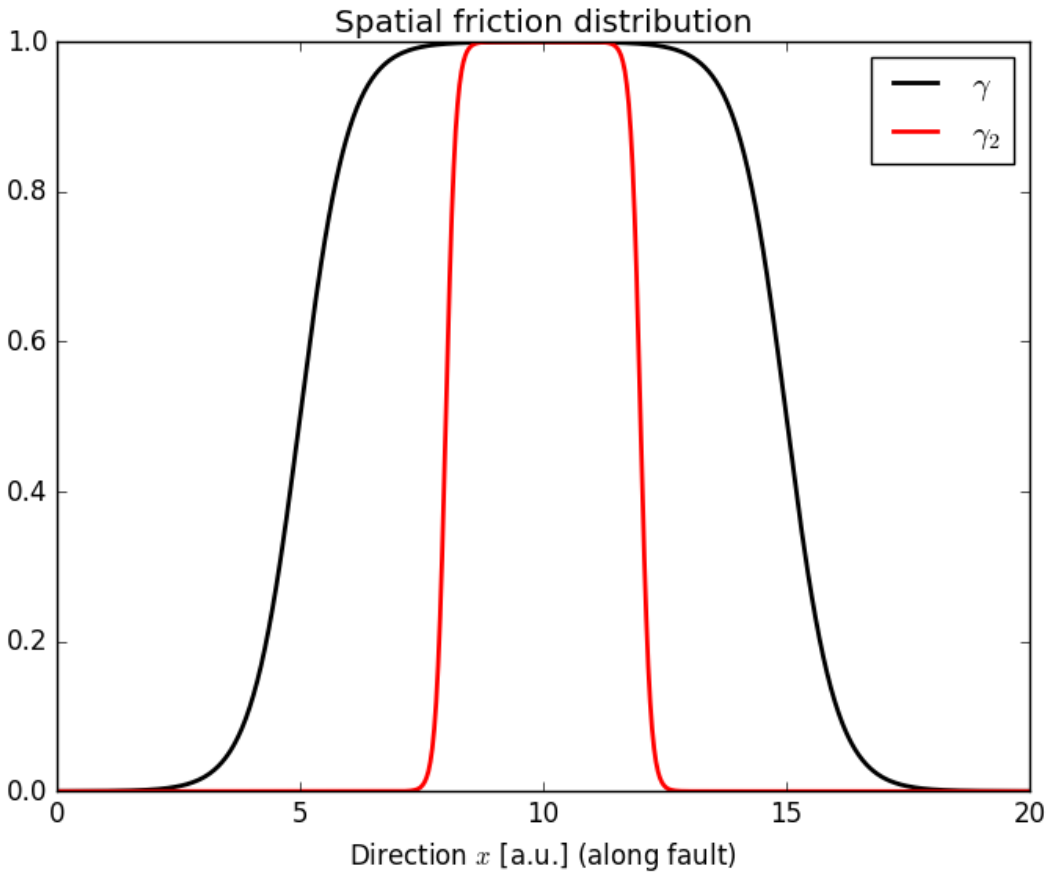
Spatial friction distribution
1.0
0.8
0.6
0.4
0.2
0.0
0
5
10
15
20
γ
γ_2
Direction x [a.u.] (along fault)

Figure 8

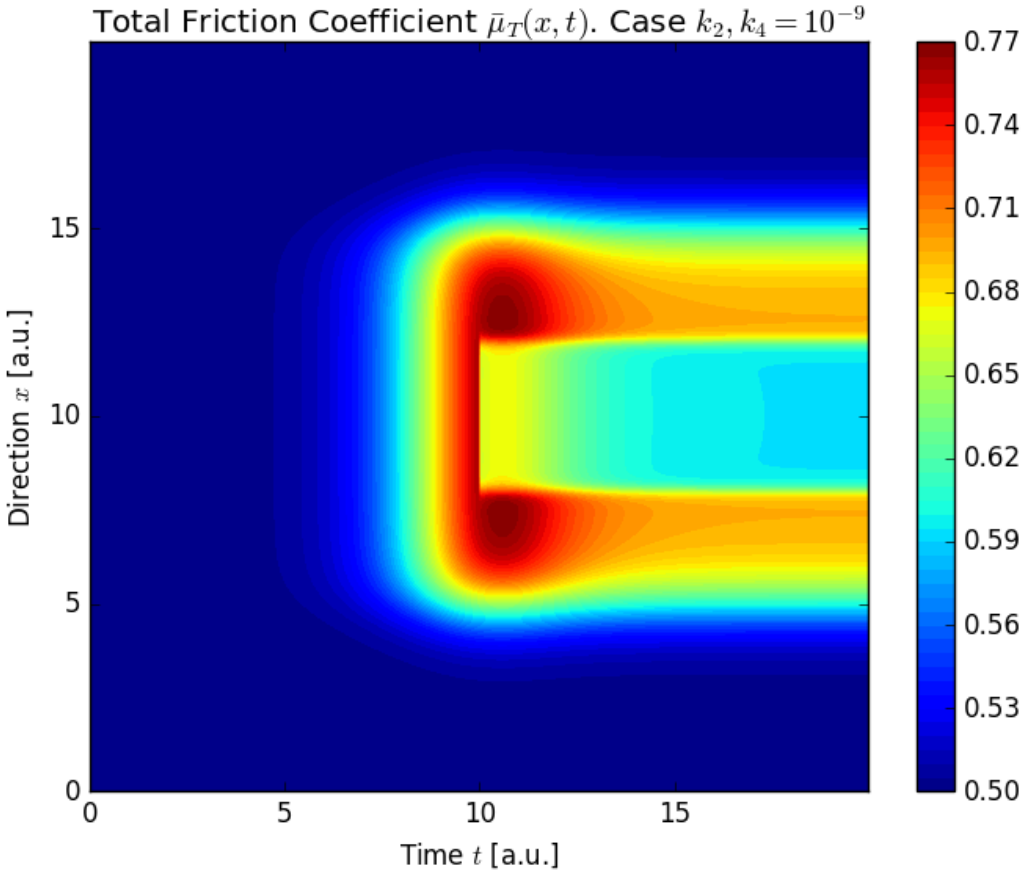
Total Friction Coefficient $\bar{\mu}_T(x,t)$. Case $k_2, k_4 = 10^{-9}$
Direction x [a.u.]
Time t [a.u.]
0
5
10
15
0.77
0.74
0.71
0.68
0.65
0.62
0.59
0.56
0.53
0.50

Figure 9

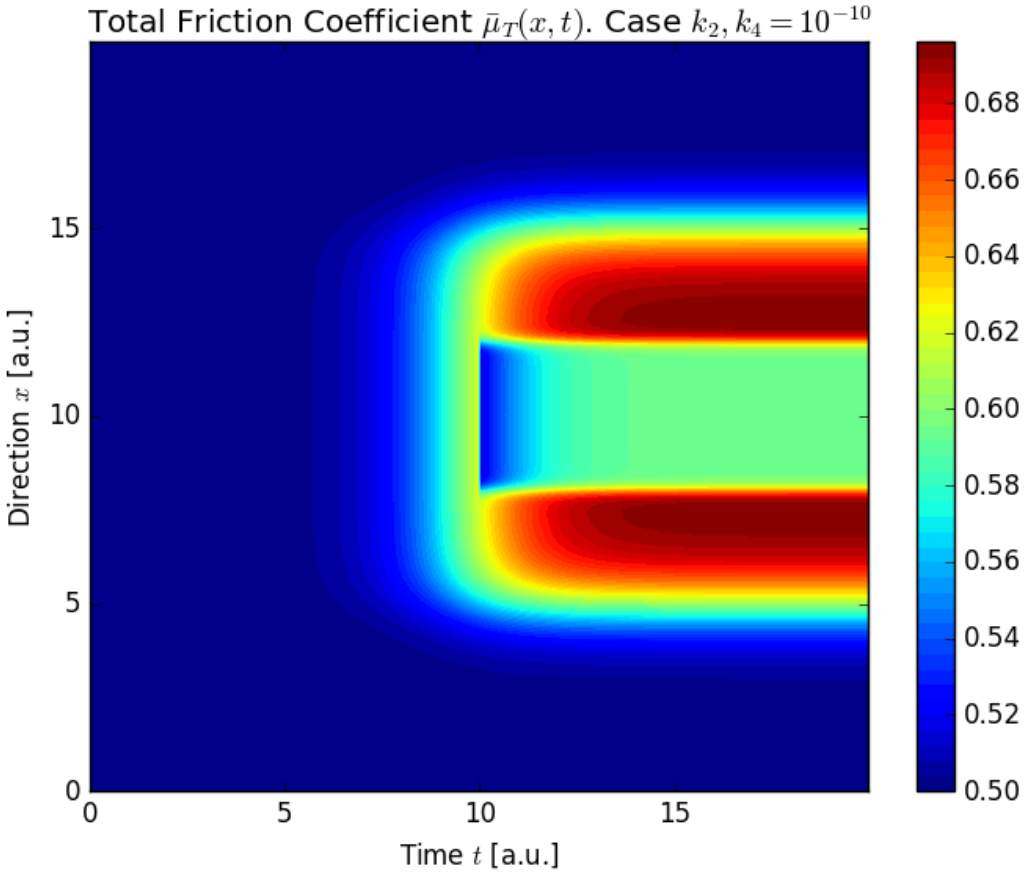
Total Friction Coefficient $\bar{\mu}_T(x,t)$. Case $k_2, k_4 = 10^{-10}$
Direction x [a.u.]
Time t [a.u.]
0
5
10
15
0.68
0.66
0.64
0.62
0.60
0.58
0.56
0.54
0.52
0.50

Figure 10

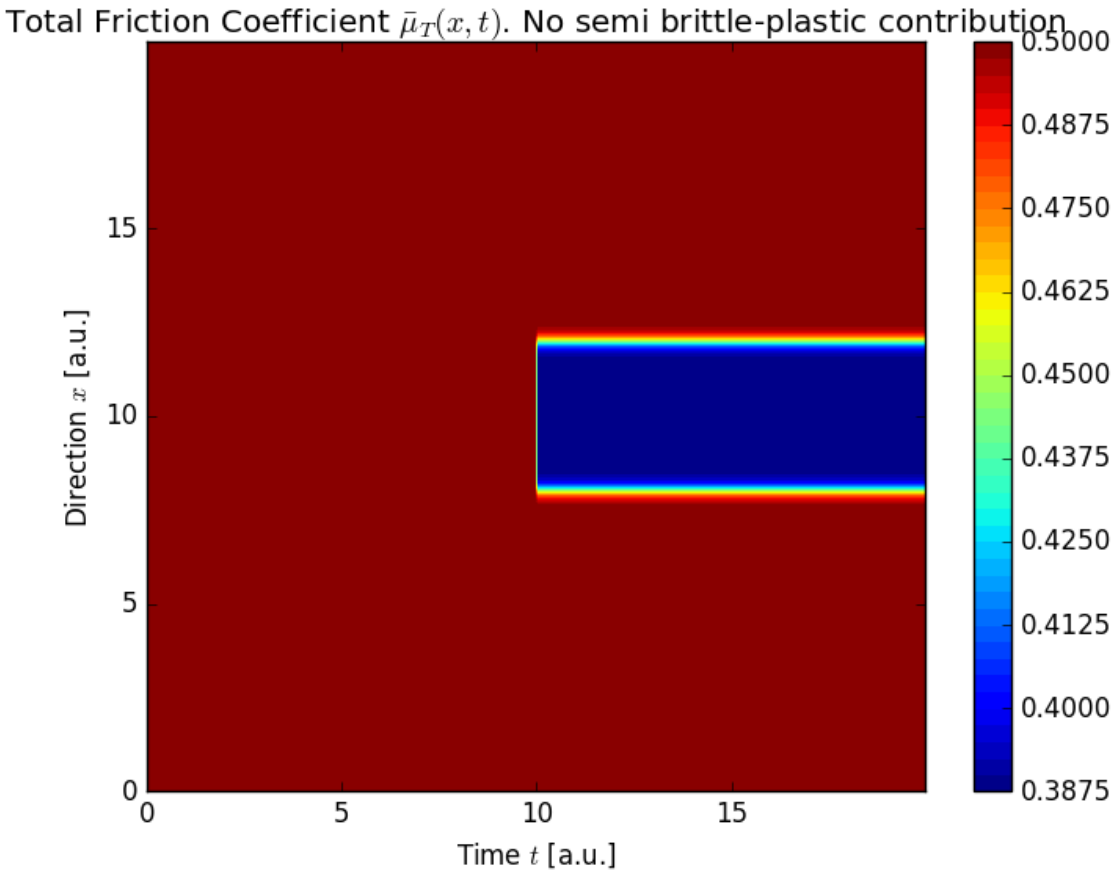
Total Friction Coefficient $\bar{\mu}_T(x,t)$. No semi brittle-plastic contribution
Direction x [a.u.]
Time t [a.u.]
0
5
10
15
0.5000
0.4875
0.4750
0.4625
0.4500
0.4375
0.4250
0.4125
0.4000
0.3875

Figure 11

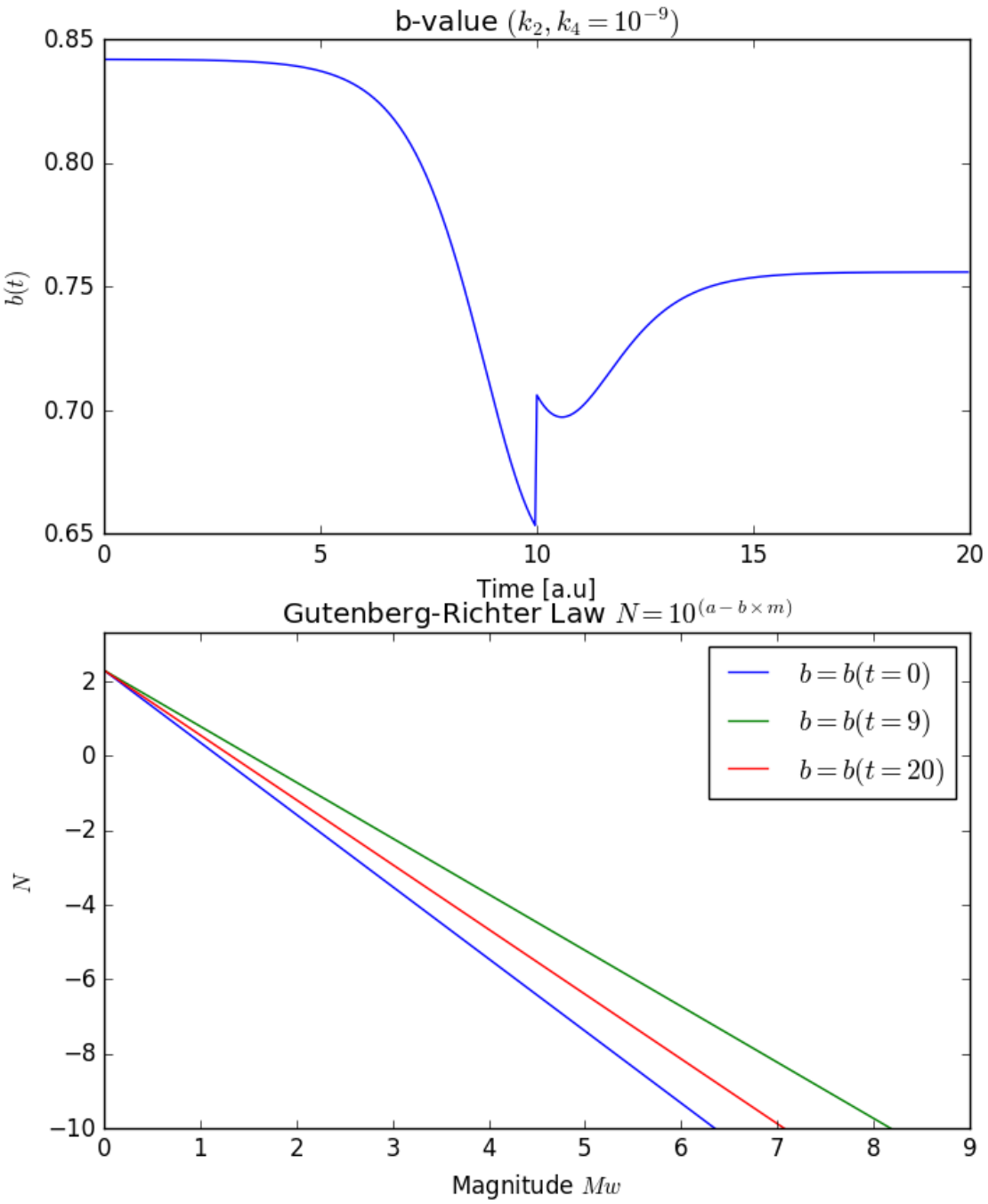
b-value $(k_2, k_4 = 10^{-9})$
0.85
0.80
0.75
0.70
0.65
$b(t)$
0
5
10
15
20
Time [a.u]
Gutenberg-Richter Law $N = 10^{(a - b \times m)}$
$b = b(t = 0)$
$b = b(t = 9)$
$b = b(t = 20)$
2
0
−2
−4
−6
−8
−10
N
0
1
2
3
4
5
6
7
8
9
Magnitude Mw

Figure 12

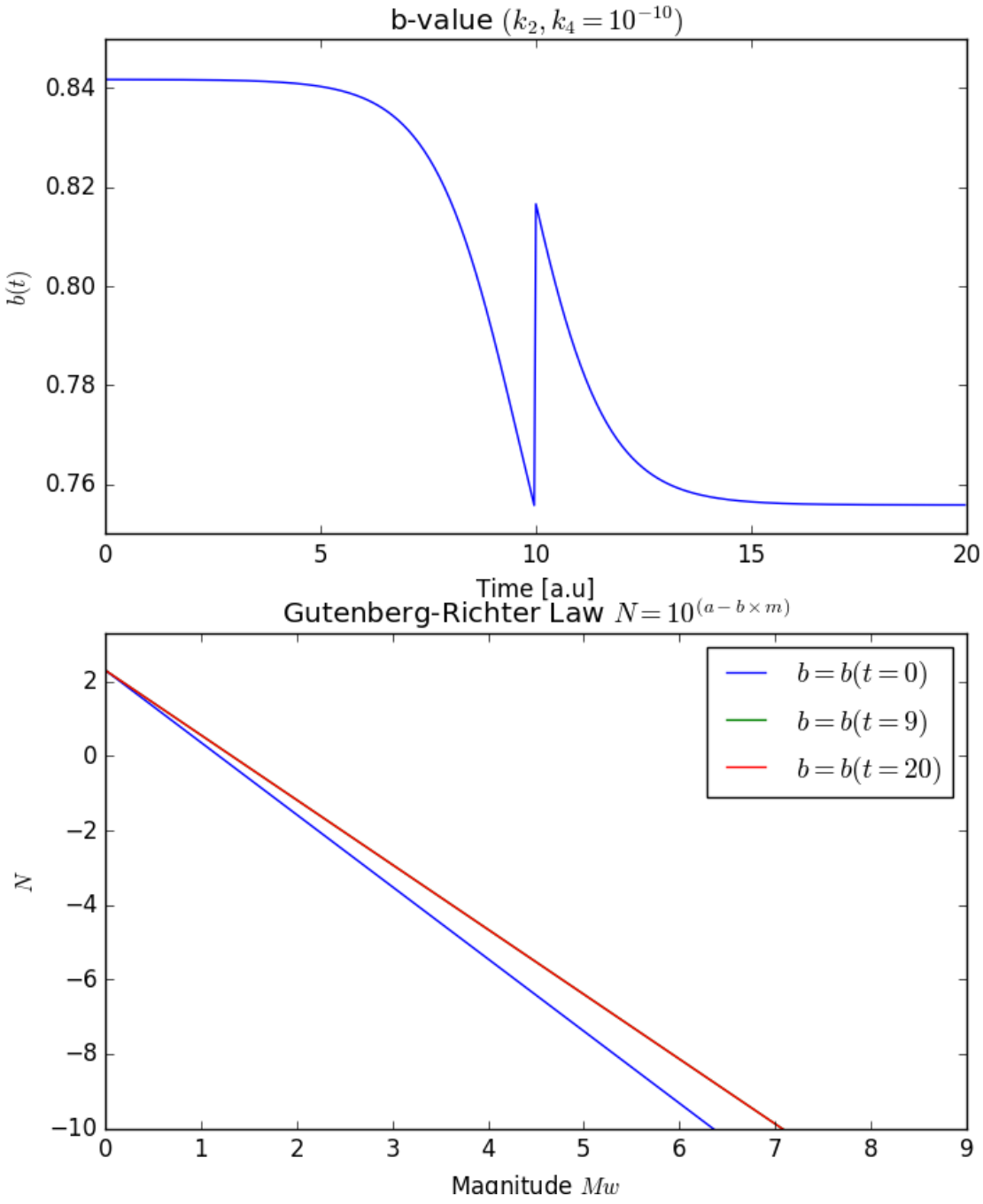
b-value $(k_2, k_4 = 10^{-10})$
0.84
0.82
0.80
0.78
0.76
$b(t)$
0
5
10
15
20
Time [a.u]
Gutenberg-Richter Law $N = 10^{(a - b \times m)}$
$b = b(t = 0)$
$b = b(t = 9)$
$b = b(t = 20)$
2
0
−2
−4
−6
−8
−10
N
0
1
2
3
4
5
6
7
8
9
Magnitude Mw

Figure 13

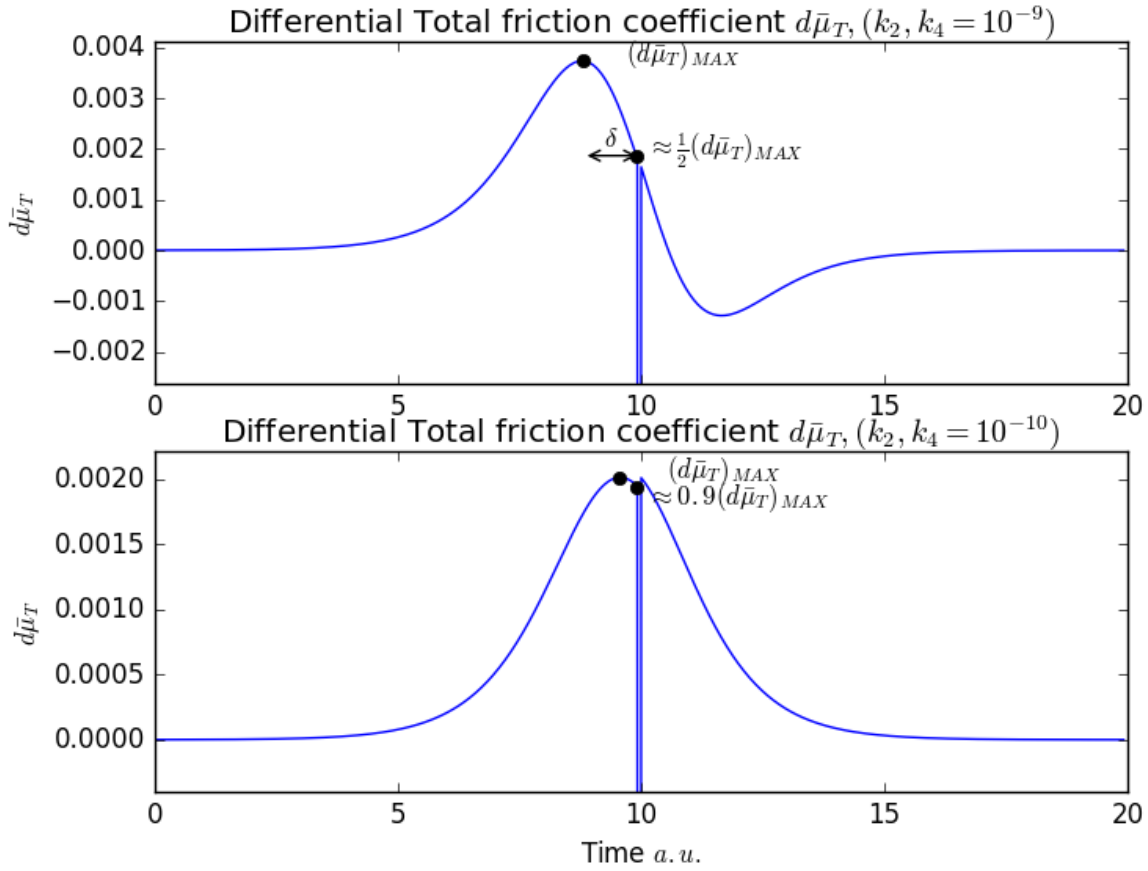
Differential Total friction coefficient $d\bar{\mu}_T, (k_2, k_4 = 10^{-9})$
$(d\bar{\mu}_T)_{MAX}$
δ
$\approx \frac{1}{2}(d\bar{\mu}_T)_{MAX}$
$d\bar{\mu}_T$
0.004
0.003
0.002
0.001
0.000
−0.001
−0.002
0
5
10
15
20
Differential Total friction coefficient $d\bar{\mu}_T, (k_2, k_4 = 10^{-10})$
$(d\bar{\mu}_T)_{MAX}$
$\approx 0.9(d\bar{\mu}_T)_{MAX}$
$d\bar{\mu}_T$
0.0020
0.0015
0.0010
0.0005
0.0000
0
5
10
15
20
Time $a.u.$